instruments

MDPI

Article

Angle-Resolved Time-of-Flight Electron Spectrometer Designed for Femtosecond Laser-Assisted Electron Scattering and Diffraction

Motoki Ishikawa [1], Kakuta Ishida [1], Reika Kanya [2,3] and Kaoru Yamanouchi [1,*]

[1] Department of Chemistry, School of Science, The University of Tokyo, 7-3-1 Hongo, Bunkyo-ku, Tokyo 113-0033, Japan
[2] Department of Chemistry, Faculty of Science, Tokyo Metropolitan University, 1-1 Minami-Osawa, Hachioji-shi, Tokyo 192-0397, Japan
[3] JST PRESTO, 1-1 Minami-Osawa, Hachioji-shi, Tokyo 192-0397, Japan
* Correspondence: kaoru@chem.s.u-tokyo.ac.jp

Abstract: We developed an apparatus for measuring kinetic energy and two-dimensional angular distributions of femtosecond laser-assisted electron scattering (LAES) signals with a high detection efficiency, consisting of a photocathode-type ultrashort pulsed electron gun, a gas injection nozzle, an angle-resolved time-of-flight analyzer, and a time-and-position sensitive electron detector. We also established an analysis method for obtaining the kinetic energy and two-dimensional angular distributions of scattered electrons from raw data of their flight times and the detected positions at the detector recorded using the newly developed apparatus. From the measurement of the LAES processes of Ar atoms in a femtosecond near-infrared intense laser field, we obtained a two-dimensional angular distribution image of the LAES signals and showed that the detection efficiency of the LAES signals was raised by a factor of 40 compared with that achieved before in 2010.

Keywords: electron scattering; differential cross sections; angle-resolved time-of-flight analyzer; laser-assisted electron scattering (LAES); laser-assisted electron diffraction (LAED)

Citation: Ishikawa, M.; Ishida, K.; Kanya, R.; Yamanouchi, K. Angle-Resolved Time-of-Flight Electron Spectrometer Designed for Femtosecond Laser-Assisted Electron Scattering and Diffraction. *Instruments* **2023**, *7*, 4. https://doi.org/10.3390/instruments7010004

Academic Editor: Antonio Ereditato

Received: 14 November 2022
Revised: 25 December 2022
Accepted: 27 December 2022
Published: 3 January 2023

1. Introduction

When an electron is elastically scattered by an atom or a molecule in the presence of a laser field, the electron can gain or lose its kinetic energy by multiples of a laser photon energy. In the past 50 years, this scattering process of an electron in a laser field called laser-assisted electron scattering (LAES) has been an attractive research target both theoretically [1] and experimentally [2–4].

In the early LAES experiments, cw-CO_2 lasers [5–8] and pulsed-CO_2 lasers with the pulse duration of microseconds [9–15] were adopted as light sources. On the other hand, considering that LAES signals carry valuable information on target atoms and molecules during a time window in which they are interacting with a light field, LAES measurements using femtosecond laser pulses were long awaited to probe ultrafast dynamical processes of atoms and molecules.

However, because the cross section of the LAES process in which a scattered electron gains or loses the energy corresponding to the one photon energy of the laser pulse is proportional to the laser field intensity (I), the laser pulse duration (Δt), and λ^4 with λ being the wavelength of the laser field [16], the intensities of LAES processes occurring in a typical near-infrared (NIR) femtosecond laser pulse with $I = 10^{12}$ W/cm^2, $\Delta t = 200$ fs, $\lambda = 800$ nm are expected to be seven orders of magnitude smaller than those of LAES processes occurring in a CO_2 laser pulse with $I = 10^9$ W/cm^2, $\Delta t = 2$ µs, and $\lambda = 10.6$ µm [9].

In 2010, LAES signals scattered by Ar atoms in a femtosecond laser field ($f = 5$ kHz, $\Delta t = 200$ fs) were recorded [17] by our group using a home-built apparatus [18] equipped

with a photocathode-type electron gun, a toroidal-type electrostatic electron energy analyzer, and a position-sensitive electron detector, which enabled us to record the energy and angular distributions of scattered electrons. This demonstration of the LAES measurements using femtosecond laser pulses drew much attention because of the potential applicability of LAES processes to ultrafast imaging of molecules [17] as well as to investigation of light-dressed states of atoms in an intense laser field [19,20].

One of the attractive applications of femtosecond LAES is laser-assisted electron diffraction (LAED) by which instantaneous geometrical structures of molecules can be probed with femtosecond temporal resolution. A LAED pattern was recorded first using carbon tetrachloride (CCl_4) as a sample gas [21] and it was confirmed that the instantaneous geometrical structure of CCl_4 during the femtosecond (~500 fs) pulse duration can be determined from a diffraction pattern appearing in the angular distributions of the LAES signals. However, considering that a long-time accumulation of the order of 10 h was necessary to record the femtosecond LAED pattern of CCl_4 with a sufficiently high signal-to-noise (S/N) ratio, it would be an extremely tough task to perform pump-probe measurements to probe a temporal evolution of the geometrical structure at many pump-probe delay times.

As summarized in a recent review [22], in the previous measurements of femtosecond LAES [17,18,23] and LAED [21], a small portion of the scattered electrons pass through a thin straight slit placed at the entrance of the toroidal-type energy analyzer analyzer, so that only ~1.4% of the scattered electrons were detected [18]. Therefore, we constructed another home-built apparatus equipped with an angle-resolved time-of-flight (ARTOF) analyzer and a time-and-position sensitive electron detector, having much larger collection efficiency of LAES and LAED signals [24].

In the present article, we examine the specifications of the second-generation LAES/LAED apparatus and report a detailed procedure for obtaining the kinetic energy and two-dimensional angular distributions of scattered electrons from raw LAES data recorded by the second-generation LAES/LAED apparatus using an Ar sample gas, while the capability of recording the angular distribution of the electron scattering signals and the improvement of the detection efficiency are examined using He and Xe as sample gases, respectively.

2. Apparatus

A schematic of the second-generation LAES/LAED apparatus is shown in Figure 1a, consisting of a photocathode-type ultrashort pulsed electron gun, a gas injection nozzle, an ARTOF-type electron analyzer, and a time-and-position sensitive electron detector (HEX-75, RoentDek Handels GmbH). An incident electron beam with the kinetic energy of 1000 eV, a pulsed femtosecond laser beam, and an effusive atomic beam, introduced continuously from a gas injection nozzle, cross at right angles at the same spatial point.

The scattered electrons pass through an entrance skimmer whose orifice diameter is 14 mmϕ, and are introduced into the ARTOF analyzer, so that the energy and angular distributions of the scattered electrons are recorded. The electrons propagating in the very small scattering angle range (<0.4°), most of which are electrons that are not scattered by a sample gas, are blocked by a beam-block wire (1 mmϕ) placed at the downstream of the entrance skimmer as shown in Figure 2a. From the arrival time (t_{TOF}) and the two-dimensional position (x, y) of each scattered electron detected by the time-and-position sensitive detector, the kinetic energies and scattering angles of the respective scattered electrons are determined. We confirm using a Xe gas as a sample gas that 54% of elastically scattered electrons in the polar angle range between 0.4° and 10° can be recorded using this apparatus, which means that the collection efficiency is raised by a factor of 39 from 1.4% achieved by the first-generation LAES/LAED apparatus [17,18].

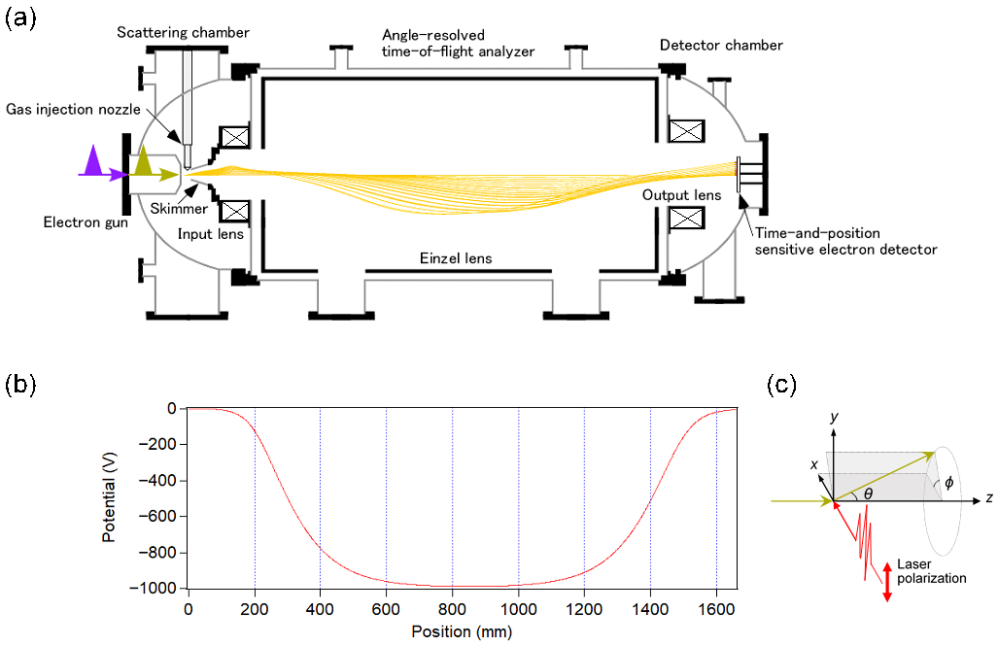

Figure 1. (**a**) The schematic of the second-generation LAES/LAED apparatus. (**b**) The electric potential along the cylindrical axis of the ARTOF tube. (**c**) The definitions of the x, y, and z axes and the polar and azimuthal angles.

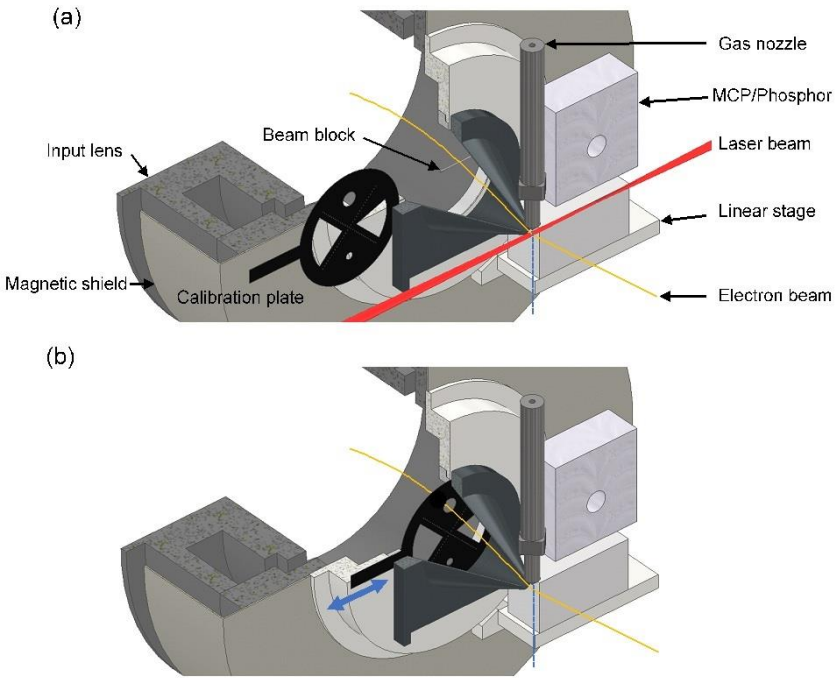

Figure 2. (**a**) An expanded view around the scattering point where the electron beam (yellow), the laser beam (red), and the atomic/molecular beam (blue broke line) cross at right angles. The scattered electrons are introduced into the ARTOF tube through the tip hole (14 mmϕ) of the entrance skimmer. (**b**) An expanded view around the scattering point when the calibration plate is inserted for the angular calibration of the electron scattering signals.

In order to monitor the electron beam profile, a microchannel plate with a phosphor screen (MCP/Phosphor) is placed at 20 mm downstream of the scattering point (See Figure 2a). This beam profile detector is mounted together with the entrance skimmer on a linear stage, by which the beam profile detector can be slid along the direction perpendicular

to the electron beam propagation direction manually from outside of a vacuum chamber, so that it is slid into the electron beam path only when the electron beam profile is monitored. Details of the respective components of the apparatus are described in Sections 2.1–2.5.

2.1. Vacuum Chambers

The apparatus consists of an interaction chamber, an ARTOF analyzer, and a detector chamber. The interaction chamber is equipped with a photocathode-type pulsed electron gun, a gas nozzle, and entrance and exit window ports for the laser beam inducing LAES/LAED processes. The ARTOF analyzer has an input electromagnetic lens (IL), an electrostatic einzel lens, and an output electromagnetic lens (OL). By the einzel lens, scattered electrons are decelerated and guided to the position sensitive detector. The electric potential along the cylindrical axis is shown in Figure 1b. The input and output magnetic lenses generate the magnetic fields having opposite polarities with respect to the electron propagation direction to minimize the rotation and the distortion of electron images recorded by the detector. In order to prevent the earth magnetic fields from affecting to the electron trajectories, the inner surface of the vacuum chambers is covered by μ-metal shields with 1 mm thickness and the vacuum chambers are laminated from outside by thin Permalloy sheets.

The interaction chamber, the ARTOF analyzer, and the detector chamber are pumped by one turbo molecular pump (TMP), two TMPs, and two TMPs, respectively. The pressures in the respective chambers are recorded using hot-cathode-type nude ion gauges. When a sample gas is not introduced, typical pressures are 5.0×10^{-6} Pa at the interaction chamber, 8.0×10^{-7} Pa at the ARTOF analyzer, and 7.0×10^{-7} Pa at the detector chamber. When a sample gas is introduced through a sample gas nozzle during LAES/LAED measurements, a needle gas valve in the sample gas line is adjusted so that the pressure inside the detector chamber is kept to be lower than 1.0×10^{-4} Pa to prevent background noises due to ion feedback at the detector, resulting in the pressures inside the interaction chamber and the ARTOF analyzer to be 1.0×10^{-3} Pa and 8.0×10^{-5} Pa, respectively.

2.2. Laser Beam

The output of a 5 kHz Ti:sapphire laser system (Δt = 40 fs, λ = 800 nm, ~0.2 mJ/pulse) is expanded by a spherical beam expander and a cylindrical beam expander, and is focused by a plano-convex lens whose focal length is f = 500 mm. The focal point is set to be 50 mm in front of the scattering point, so that the horizontal and vertical beam sizes at the scattering point are 0.7 mm and 2.0 mm in $1/e^2$ diameter, respectively, which ensure a sufficiently large spatial overlap of the laser pulse with the electron and sample gas beams. The peak laser-field intensity at the scattering point is estimated to be $I = 9.0 \times 10^{11}$ W/cm^2. The polarization vector of the laser field is set to be parallel to the propagation direction of the sample gas beam.

2.3. Sample Gas Beam

The effusive and continuous sample gas beam is introduced into the interaction chamber through a nozzle along the vertical direction and crosses at right angles with the electron beam and the laser beam. The nozzle whose orifice diameter is 0.4 mm is mounted on a *xyz*-stage. A thin gold wire (100 μmϕ) is mounted on the nozzle unit so that the wire is on the nozzle axis as shown in Figure 3a to secure a spatial and temporal overlap between the laser pulse and the electron pulse [18]. The width of the sample gas density distribution is measured by recording the intensity of the electrons elastically scattered by Ne atoms as a function of the position of the nozzle whose position is scanned horizontally along the laser beam axis. From a least-squares fit of the result of the scan shown in Figure 3b to a Gaussian function, the full-width at half-maximum of the sample density distribution is determined to be 1.3 mm.

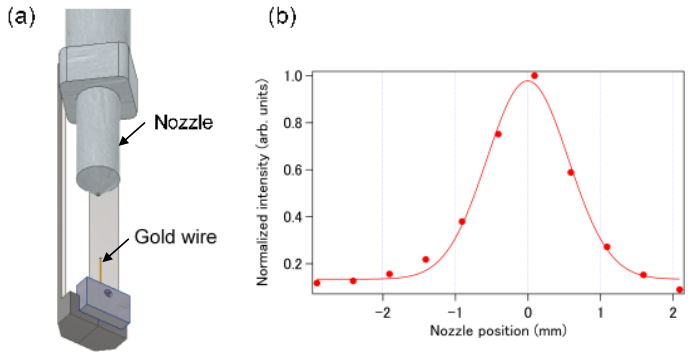

Figure 3. (**a**) An expanded view of the nozzle unit to which a thin gold wire for the adjustment of the horizontal position of the nozzle. (**b**) The normalized signal intensity of the electrons elastically scattered by Ne atoms plotted as a function of the horizontal nozzle position along the direction parallel to the laser beam. Filled circles: experimental results. Solid curve: a best-fit Gaussian function.

2.4. Electron Beam

The structure of the photocathode-type pulsed electron gun whose cross section is shown in Figure 4 is basically the same as that of the first-generation apparatus described in Ref. [18]. The photocathode is made of a quartz plate whose anode side surface is coated with an Au layer whose thickness is 10 nm. An electron pulse is generated by the photoelectric effect induced by irradiation of the Au photocathode surface with a UV laser pulse (λ = 267 nm, Δt = 20 ps, I = 5 pJ/pulse) focused by a spherical lens (f = 350 mm). The UV pulses are generated as the third harmonic of chirped fundamental 200 ps pulses that are partially split from the amplified laser pulse before the pulse compressor of the laser system. Because of the restricted conversion bandwidth of the first SHG crystal with 0.4 mm thickness, 20 ps pulses are generated from broadband chirped 200 ps pulses. The cathode voltage (−1000 V) is applied to the Au surface of the photocathode and the generated electrons are accelerated up to 1000 eV in the 0.3 mm gap between the photocathode and the grounded anode, and the electron pulse passing through a 0.1 mmϕ pinhole located at 6.0 mm downstream of the photocathode is collimated by using the electromagnetic lens in the electron gun. In the electron gun, an electromagnetic octupole deflector located just after the electromagnetic lens deflects the collimated electron beam by 10°, so that the electron beam axis coincides with the symmetric axis of the ARTOF analyzer. This slightly off-axis configuration of the initial direction of the electron beam with respect to the symmetric axis of the ARTOF analyzer prevents the UV pulse transmitted through the photocathode from hitting the electron detector located at the end of the ARTOF analyzer. The magnetic octupole deflector is also used for the adjustment of the electron beam profile.

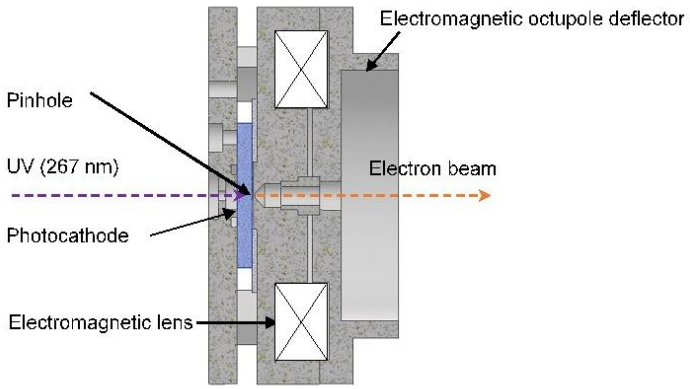

Figure 4. The cross section of the photocathode-type pulsed electron gun.

The number of electrons per pulse is optimized by the adjustment of the intensity of the UV laser pulse so as not to increase the energy spread of the electron beam induced by the space-charge effect. The typical energy of the UV pulse is ~8 pJ/pulse, and the number of electrons per pulse is estimated to be $<10^3$ from the quantum efficiency of a gold film [25]. The electron beam diameter at the scattering point is measured by the knife edge scan method [18], in which the electron signal intensity monitored by the MCP/Phosphor slid into the electron beam path is recorded as a function of the position of the nozzle tip, acting as a knife edge. From this measurement, the vertical and horizontal sizes of the electron beam at the scattering point are determined to be 300 ± 1 μm in $1/e^2$ diameter.

2.5. Electron Energy Analyzer and Detector

As shown schematically in Figure 1a, the ARTOF analyzer consists of the input electromagnetic lens, the flight tube with the inner diameter of 500.0 mm, and the output electromagnetic lens. The grounded input and output electromagnetic lenses are operated at the electric current of 75 and 90 mA, respectively, and the voltage of the flight tube is set to be at −995 V, so that the two electromagnetic lenses and the flight tube form an einzel lens. The scattered electrons propagating towards the detector located 1660 mm downstream of the scattering point are decelerated down to ~10 eV around the central region of the flight tube, so that the kinetic energy shift of the scattered electrons is magnified as a form of their time-of-flights to be recorded by the detector. The electrons are then reaccelerated up to their original energy and detected by the time-and-position sensitive electron detector.

In order to resolve an energy shift structure of the scattered electrons originating from a LAES process, the scattered electrons whose kinetic energies are around 1 keV need to be recorded with sufficiently higher energy resolution than 1.55 eV, corresponding to the amount of the one-photon energy of an 800 nm light field. Therefore, voltages generated by high-precision low-voltage regulating circuits having only small ripples of ± 20 mV_{pp}, which are floated on a common high voltage of −1000 V, are applied to the photocathode of the electron gun and to the flight tube of the analyzer.

We obtained the LAES signals by accumulating the scattered electrons for 100 s alternatingly with and without a temporal overlap between the electron pulse and the laser pulse and subtracted the accumulated signals without the temporal overlap from the accumulated signals with the temporal overlap. We repeated a set of the alternating accumulation many times, each of which takes a total of 213 s including the time (13 s) required for the delay stage translation, to increase the S/N ratio of the LAES signals. By this accumulation scheme, the effect of temporal fluctuations in the experimental conditions such as the fluctuations in the laser peak intensity and pulsed electron beam intensity are compensated. During the accumulation with no temporal overlap between the laser pulse (Δt = 40 fs) and the electron pulse (Δt = 20 ps), the temporal delay of the laser pulse with respect to the electron beam pulse is set to be 66 ps to secure the no temporal overlap conditions. We accumulated the signals for 19 h, during which 302 cycles were repeated, so that the net accumulation time was 16.8 h.

3. Data Analysis

In order to obtain the scattering angles, (θ, ϕ), and the energy shift, ΔE, from a raw data set of (x, y, t_{TOF}) for the position (x, y) and the arrival time (t_{TOF}) of an electron detected by the time-and-position sensitive detector, we adopted a two-step procedure, in which ΔE is obtained first from (x, y, t_{TOF}), and then, (θ, ϕ) are obtained from the data set of (x, y, ΔE).

3.1. Determination of ΔE

To convert (x, y, t_{TOF}) to ΔE, we performed measurements of elastic scattering signals of electrons, accelerated to given kinetic energies for the calibration and scattered by a Ne sample gas beam. In the measurements, no laser pulses were introduced at the electron-Ne scattering and the count rate of scattered electrons was kept to be around 100 cps so that the broadening of the TOF spectrum originating from the space charge effect is

suppressed. As the acceleration voltages, we chose five different values of 996.90 eV, 998.45 eV, 1000.00 eV, 1001.55 eV, and 1003.10 eV, corresponding to 1000 + $n\Delta E_{\mathrm{calib}}$ eV (n = 0, ±1, ±2) with $\Delta E_{\mathrm{calib}}$ being the one photon energy (1.55 eV) of the 800 nm laser field used in the LAES experiments. In the calibration process, (x, y) are expressed by grid points, (x_n, y_m), representing a binned area whose pixel size is 500 nm × 500 nm. Note that the origin of the x-y coordinate system is set to be approximately at the center of the detector, but a position (x_c, y_c) where the pulsed electron beam hits on the x-y plane is in general slightly off from the origin of the coordinate system.

For example, the distributions of t_{TOF} of electrons elastically scattered by a Ne sample gas recorded at (x_n, y_m) = (5 mm, −5 mm) are shown in Figure 5a, which were obtained after continuous accumulation for one hour for the five different acceleration voltages, 996.90 eV (blue), 998.45 eV (green), 1000.00 eV (yellow), 1001.55 eV (orange), and 1003.10 eV (red). In the measurements, a Ne gas was adopted so that a sufficiently large count rate can be achieved while the broadening of the TOF spectrum was kept being suppressed.

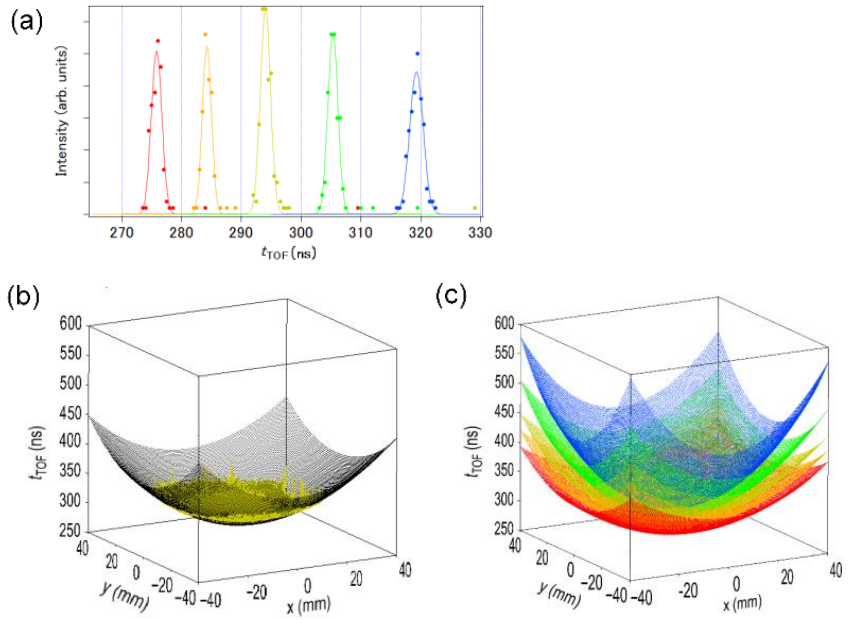

Figure 5. (**a**) The distributions of t_{TOF} for electrons scattered by Ne atoms and detected at (x, y) = (5 mm, −5 mm) on the time-and-position sensitive detector at the incident electron kinetic energies of E_i/eV = 1000 + 1.55 n with n = +2 (red), n = +1 (orange), n = 0 (yellow), n = −1 (green), and n = −2 (blue). The solid curves represent best-fit Gaussian curves to the recorded data represented by the dots. (**b**) The position dependence of the mean value of t_{TOF} at E_i = 1000 eV. Each one of the yellow dots represents the mean value of t_{TOF} obtained as the center of the best-fit Gaussian curve. The meshed surface (black) is a smoothed surface constructed using the yellow dots. (**c**) Smoothed surfaces for the position dependence of the mean values of t_{TOF} at the five different incident electron kinetic energies for n = +2 (red), n = +1 (orange), n = 0 (yellow), n = −1 (green), and n = −2 (blue).

The yellow solid line in Figure 5a for the acceleration voltage of 1000 eV with $\Delta E_{\mathrm{calib}}$ = 0 is a best-fit curve for the experimental data obtained by a least-squares analysis using a Gaussian model function. After determining t_{TOF} as the center of the best-fit Gaussian function, the distribution of t_{TOF} was plotted as a yellow dot in the 3D space at (x, y, t_{TOF}) = (5 mm, −5 mm, t_{TOF}). The same analyses were made for all the grid points and plotted to form the convex-downward surface shown in Figure 5b. The black meshed surface in Figure 5b is a smoothed convex-downward surface composed of the yellow dots representing all the grid points. The convex-downward shape reflects the fact that, at a given electron kinetic energy, the electrons scattered elastically in the larger polar angle (θ) range take the longer flight time to reach the detector because of the longer trajectories. For the other four kinetic energies of the incident electrons of 996.90 eV, 998.45 eV, 1001.55 eV,

and 1003.10 eV, their convex-downward surfaces in the 3D (x, y, t_{TOF}) space are obtained as shown in Figure 5c by the same procedure as that described above for the kinetic energy of 1000 eV.

Because t_{TOF} depends not only on the detected position (x, y) but also on ΔE, we assume that t_{TOF} can be expressed in terms of ΔE as

$$t_{TOF} = K_0(x_m, y_n) + K_1(x_m, y_n)\,\Delta E + K_2(x_m, y_n)\,\Delta E^2, \quad (1)$$

where $K_i(x_m, y_n)$ is the position dependent coefficient for the i-th order term (i = 0, 1, 2). The filled circles in Figure 6a represent the t_{TOF} values near the bottom of the convex-downward surfaces in Figure 5c for the five values of ΔE and the black solid curve represents a best-fit curve obtained by the least-squares fit to Equation (1), showing that the energy dependence of t_{TOF} is described well by the second-order polynomial expansion of Equation (1). The data set of the coefficients, $K_i(x_m, y_n)$, are determined by the fitting for the respective positions (x_m, y_n), and are stored as coefficient tables for the later analyses of recorded data. The (x, y) dependences of the $K_0(x, y)$, $K_1(x, y)$, and $K_2(x, y)$ values are plotted in Figure 6b–d, respectively. When an electron was detected at (x, y), so that it satisfied $(x, y) = (x_m + u\Delta x, y_n + v\Delta y)$ with $0 \le u < 1$, $0 \le v < 1$, the corresponding coefficients were evaluated by the bilinear interpolation method expressed as

$$K_i(x, y) = \begin{pmatrix} 1-u & u \end{pmatrix} \begin{pmatrix} K_i(x_m, y_n) & K_i(x_m, y_{n+1}) \\ K_i(x_{m+1}, y_n) & K_i(x_{m+1}, y_{n+1}) \end{pmatrix} \begin{pmatrix} 1-v \\ v \end{pmatrix} \quad (2)$$

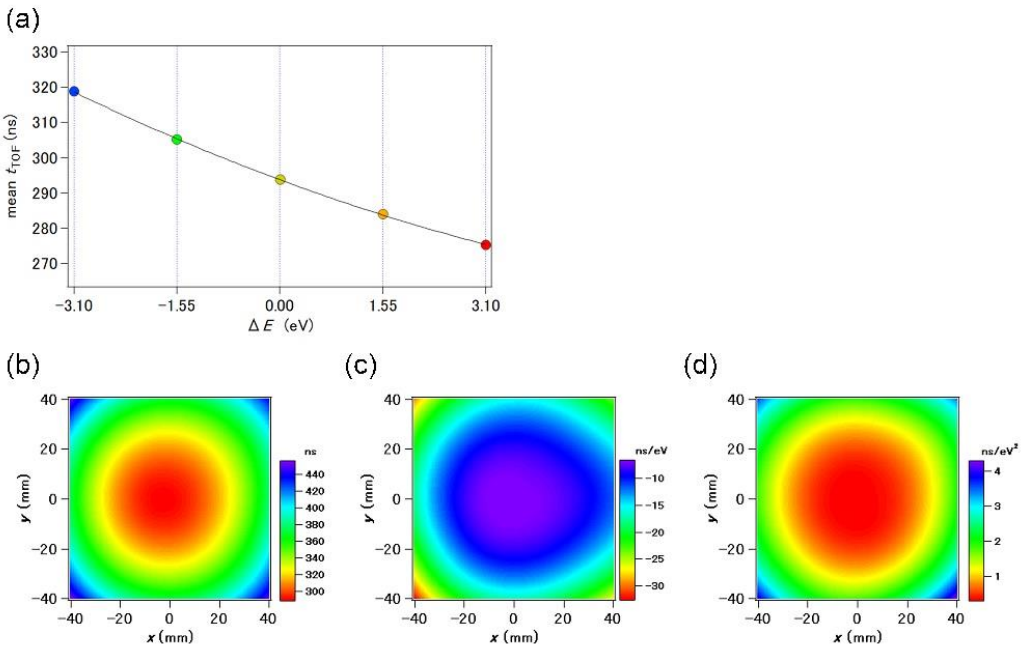

Figure 6. (**a**) Dependence of the mean values of t_{TOF} of the electrons scattered by Ne atoms at (x, y) = (5 mm, −5 mm) on the incident electron kinetic energy. Filled circles with different colors are the mean t_{TOF} values at E_i/eV = 1000 + 1.55 n with n = +2 (red), n = +1 (orange), n = 0 (yellow), n = −1 (green), and n = −2 (blue). A black solid curve represents a best-fit curve represented by the second-order polynomial expansion of Equation (1). (**b**–**d**) Position dependences of the coefficients, (**b**) $K_0(x_m, y_n)$, (**c**) $K_1(x_m, y_n)$, and (**d**) $K_2(x_m, y_n)$, in the second order polynomial (Equation (1)).

By using this quadratic formula of Equation (1), ΔE can be determined from a data set of (x, y, t_{TOF}) as

$$\Delta E = \frac{-K_1(x, y) + \sqrt{K_1^2(x, y) - 4K_2(x, y)(K_0(x, y) - t_{\mathrm{TOF}})}}{2K_2(x, y)} \tag{3}$$

3.2. Determination of θ and ϕ

As the next step, the scattering angles, (θ, ϕ), are determined from the data set of $(x, y, \Delta E)$ obtained above. By deflecting the electron beam slightly so that a part of unscattered electrons is recorded by the detector, the position of the scattering center ($\theta = 0$) on the x-y coordinate system is determined. It is found that the central position is located at $(x_c, y_c) = (-4.22$ mm, -1.18 mm) and the position does not change in the kinetic energy range of -4 eV $\leq \Delta E \leq 4$ eV, which means that, for example, the position (5 mm, -5 mm) is slightly off from the scattering center, and the x' and y' coordinates in the x'-y' coordinate system whose origin is the scattering center become $(x', y') = (9.22$ mm, -3.82 mm) after the displacement of the origin to the scattering center.

By setting (x_c, y_c) at the origin of the polar coordinate system, the position (x', y') at which an electron is detected is expressed in the r-ϕ polar coordinate system, where r is the radial coordinate and ϕ is the polar angle. Note ϕ is the azimuthal angle, but it can be regarded as the polar angle when the 2D plane spanned by the x and y coordinate is represented in the polar coordinate system and that x' and y' are represented as $x' = r\cos\phi$ and $y' = r\sin\phi$ using the polar coordinates, r and ϕ. Because of the image rotation induced by the input and output electromagnetic lenses, ϕ has an offset at the polar coordinate system on the detector surface. This offset angle was determined by the knife edge scan method, where the entrance skimmer moving horizontally acts as a knife edge for the scattered electrons.

The relation between r and θ was determined using a calibration plate made of an aluminum disk (80.0 mmϕ) with the thickness of 0.1 mm. As shown in Figure 2b, the calibration plate mounted on a movable stage is located 80 mm downstream of the scattering point. The calibration plate has a series of holes with 0.5 mm diameter along the two straight lines crossing at right angles at the center. The surface of the calibration plate is coated by graphite to avoid the charge-up on the aluminum oxide layer. The calibration plate is slid into the path of the scattered electrons using the movable stage so that its center is adjusted to be at the axis of the pulsed electron beam. The adjustment was made using the shadow image of the tip of the beam block and the calibration plate.

The distance of the neighboring holes along the straight lines is 2.0 mm, so that the scattering angle θ of the scattered electrons passing through the respective holes are determined. Figure 7a shows a typical image of the scattered electrons at $E_i = 1000$ eV passing through the small holes of the calibration plate. The radius r of the scattered electron signals at the detector is expressed using the scattering angle θ, determined by the position of the image of the holes in the calibration plate, as shown in Figure 7b at $E_i = 1000$ eV. The black solid curve in Figure 7b is the best fit curve obtained by the least-squares analysis using a fitting curve represented by the second order polynomial expansion,

$$R = L_1(\Delta E)\,\theta + L_2(\Delta E)\,\theta^2, \tag{4}$$

where $L_1(\Delta E)$ and $L_2(\Delta E)$ are the variable parameters depending on ΔE. This least-squares fits were also performed at incident kinetic energies of $E_i = 1000 + \Delta E = 1000 + 1.55\,n$ eV ($n = \pm 1, \pm 2$) to obtain the dependence of the two coefficients, $L_1(\Delta E)$ and $L_2(\Delta E)$, on the kinetic energy of the electrons.

To obtain angular distributions of LAES with n-photon energy shift, the polar scattering angles θ were calculated by solving Equation (4) about θ, and the LAES signals in the energy range around the LAES peaks satisfying $|\Delta E - n\hbar\omega| < 0.5$ eV were integrated.

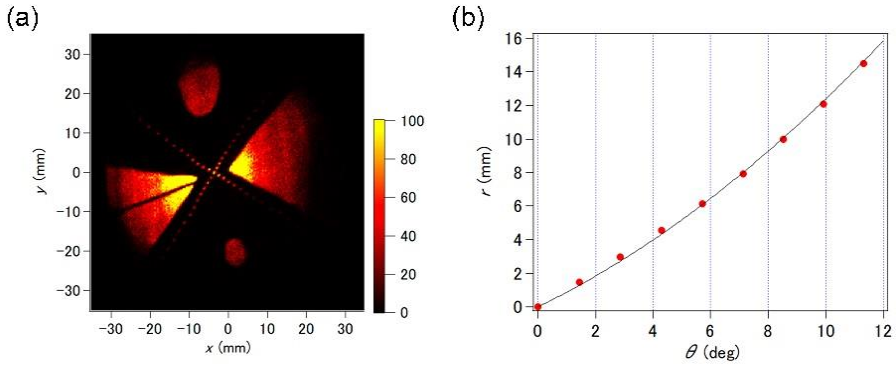

Figure 7. (**a**) An image of the elastic scattering signals of electrons scattered by Ne atoms and passing through the calibration plate at the incident electron kinetic energies of E_i = 1000 eV. (**b**) The radius R of the signals measured from $(x', y') = (0, 0)$ on the time-and-position sensitive detector as a function of the scattering angle θ at the incident electron kinetic energies of E_i = 1000 eV. A black solid curve represents a best-fit curve represented by the second order polynomial expansion of Equation (4).

3.3. Correction of Inhomogeneity of the Detector Sensitivity

In general, a two-dimensional imaging detector has a certain inhomogeneity in the detection sensitivity, that is, depending on the position on the detector surface, the detection sensitivity varies. We performed the calibration of the spatial inhomogeneity in the detection sensitivity by comparing elastic scattering signals recorded using a He gas sample with the corresponding literature values of the differential cross section of He [26]. The signals of electrons elastically scattered by He were accumulated for 20 min at a relatively low signal count rate of 70 cps, so that multiple hit events on the detector were avoided. The raw image data were converted through a binning procedure into the signal count distribution represented in the polar coordinate system, $N(r_m, \phi_n)$, with the pixel size of $(\Delta r, \Delta\phi)$ = (1.2 mm, 15°), which is sufficiently smaller than a typical scale of the spatial variation of the inhomogeneity in the detection sensitivity.

The correction factor for the respective pixels, $D(r_m, \phi_n)$, is determined by

$$D(r_m, \phi_n) = \frac{d\sigma_{el}(\theta_m, \phi_n)/d\Omega}{N(r_m, \phi_n)(\partial r/\partial\theta)} \quad (5)$$

where $d\sigma_{el}/d\Omega$ is the literature value of the differential cross section of the elastic scattering of He and $\partial r/\partial\theta$ is a conversion factor calculated to be $\partial r/\partial\theta = L_1 + 2L_2\,\theta$ using Equation (4).

4. Performance of Home-Built Apparatus

We performed the electron scattering experiments using a He gas sample in the absence of the laser fields to demonstrate the performance of the home-built apparatus. Based on the results of the measurements, we discuss possible procedures for increasing a signal count rate.

4.1. Angular Distribution of the Scattered Electrons

The recorded signals of electrons elastically scattered by a He gas sample in the absence of the laser fields are shown in Figure 8a. The dark thin bar extending from the left side to the center is the shadow of the beam-block wire (1 mmϕ) placed after the entrance skimmer of the ARTOF analyzer. The differential cross section of the elastically scattered electrons by He were obtained using the recorded scattering signals shown in Figure 8b with the sensitivity correction represented by Equation (7). From the comparison with literature values of the differential cross section of He [22] shown by a black solid line, we confirmed that the detector can be used for the detection of the electron signals scattered in the polar angular range of $1.8° \leq \theta \leq 10°$. The smaller polar angle range of $\theta \leq 1.8°$ is influenced by the beam block.

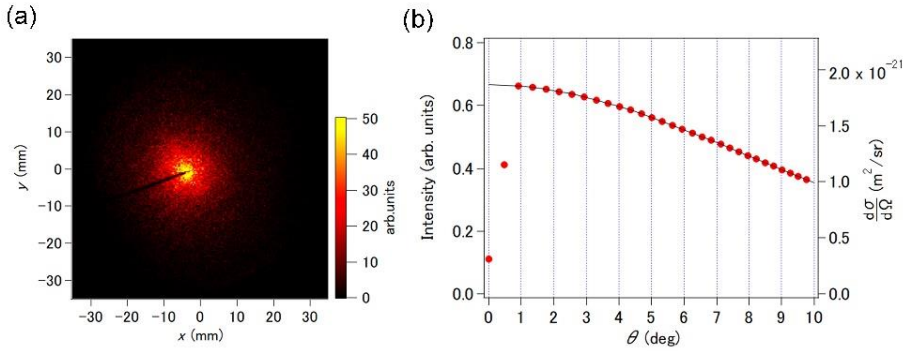

Figure 8. (**a**) An image of the scattering electrons at the incident electron kinetic energies of E_i = 1000 eV scattered by He atoms in the absence of laser fields. (**b**) Experimental differential cross sections (DCSs) (red filled circles) and a theoretically calculated DCS curve [26] (black solid curve) for electrons elastically scattered by He atoms.

4.2. Signal Count Rate

In order to compare the signal count rate achieved by the present measurements with that achieved by our first-generation apparatus, we recorded the signals of electrons scattered by a Xe gas sample and confirmed that the signal count rate of the elastically scattered electrons is 830 cps. Even though the sample gas density in the present measurements was only 20% of that in our previous experiment using the first-generation apparatus [18], the count rate is larger by a factor of 9.2. Therefore, the signal count rate can be raised by a factor of about 40 if the sample gas density is increased by a factor of 5, which is consistent with the factor of 39 estimated from the difference in the acceptance angle.

The sample gas density can be raised more by an improvement in the vacuum system. For operating the detector, the pressure in the detector chamber needs to be lower than 1×10^{-4} Pa, so that the ion feedback at the detector is avoided, and this critical pressure limits the maximum amount of the sample gas flow from the nozzle. A promising way to raise the gas flow without raising the pressure in the detector chamber is to make the diameter of the entrance skimmer placed at the entrance of the flight tube smaller. The maximum gas flow is allowed to be increased inversely proportional to the area of the hole. Because the current diameter of the skimmer hole is 14 mm, if the diameter is reduced to 6 mm, the gas flow can be raised by a factor of five. Even when the size of the hole is made smaller, by setting the tip of the skimmer closer to the scattering point, the detectable angular range can be maintained.

Another way of increasing the signal count rate is to make the width of the beam block wire thinner. As described above, the detectable angular range of the scattered electrons is $1.8^\circ \leq \theta \leq 10^\circ$ and the signals of scattered electrons in the scattering angle range of $\theta < 1.8^\circ$ cannot be used because of the effect of the beam block wire. According to the literature values of the differential cross section of the elastic electron scattering by He atoms [26], the scattering cross section in the scattering angle range of $0^\circ \leq \theta \leq 1.8^\circ$ is around 30% of that in the range of $0^\circ \leq \theta \leq 10^\circ$. Therefore, the signal count rate can be increased by the measurement using a thinner beam block wire.

4.3. Kinetic Energy Spectra and LAES Signals

We performed the measurements of LAES processes for Ar using the second-generation apparatus. A continuous Ar gas beam, a linearly polarized NIR laser pulses ($I = 9.0 \times 10^{11}$ W/cm^2, λ = 800 nm, ~0.2 mJ/pulse, Δt = 40 fs, f = 5 kHz), and a pulsed electron beam (1 keV, Δt = 20 ps, f = 5 kHz) cross at right angles at the scattering point.

The recorded kinetic energy spectra of the electrons scattered by Ar atoms in the polar scattering angle range of $1.8^\circ \leq \theta \leq 10^\circ$ are shown in Figure 9a. The spectrum recorded when the electron pulse and the laser pulse are temporally overlapped at the scattering point, hereafter called the spectrum with the temporal overlap, is plotted with red filled circles and that recorded when the laser pulse is delayed by 66 ps with respect to the

electron pulse, hereafter called the background spectrum, is plotted with black open circles. The two spectra are normalized by the peak height of the elastic scattering signals without the temporal overlap.

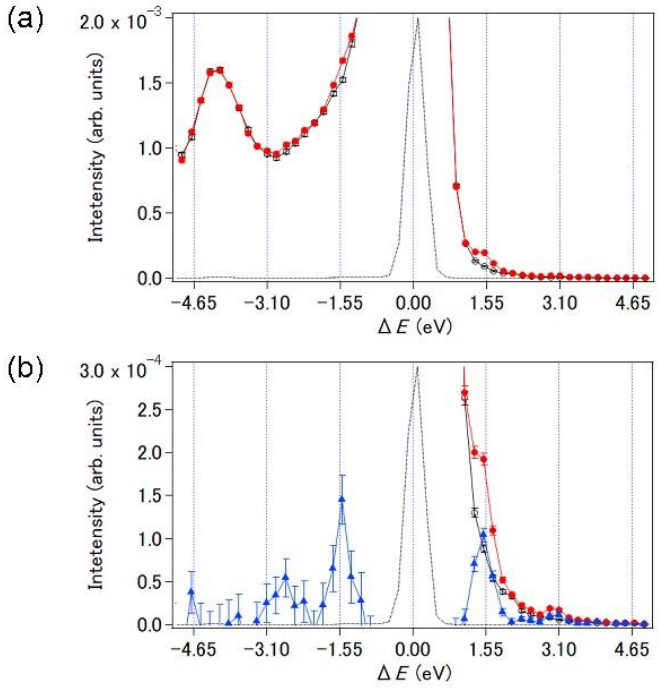

Figure 9. (**a**) The kinetic energy spectrum of the scattering intensity of electrons scattered by Ar atoms recorded with the laser pulses temporary synchronized with the electron pulses (red filled circles with error bars) and that recorded when the laser pulses pass through the scattering point 66 ps after the electron pulses (black open circles with error bars). A black dotted line represents the background electron signal intensity multiplied by 2.0×10^{-3} recorded without the temporal overlap. (**b**) The difference kinetic energy spectrum (blue filled triangles) obtained by subtracting the electron scattering signals without the temporal overlap between the electron and laser pulses (black open circles) from those with the temporal overlap (red filled circles with error bars). The two peaks appearing in the spectrum plotted with the blue filled triangles at $\Delta E = -1.55$ and 1.55 eV represent the LAES signals at $n = -1$ and +1, respectively. A black dotted line represents the background electron signal intensity multiplied by 3.0×10^{-4} recorded without the temporal overlap.

In the expanded view shown in Figure 9b, an increase in the signal intensity can be seen at around $\Delta E = 1.55$ eV in the spectrum with the temporal overlap, which cannot be seen in the background spectrum. In order to see more clearly the difference in Figure 9b, we subtracted the background spectrum from the spectrum with the temporal overlap. The resultant difference spectrum plotted with blue filled triangles exhibits peaks at $\Delta E = -1.55$, +1.55 and +3.10 eV, which can be assigned to the LAES signals for $n = -1$, +1, and +2.

The relative intensities of the LAES peaks to the central elastic peak ($n = 0$) are 1.0×10^{-4} for $n = +1$, 1.2×10^{-5} for $n = +2$, and 1.4×10^{-4} for $n = -1$. These relative intensities are consistent with the theoretical values of 1.1×10^{-4} for $n = \pm 1$, 1.3×10^{-5} for $n = \pm 2$ obtained by the differential cross section formula given by Kroll-Watson [16] using the experimental conditions of the temporal and spatial overlap among the three beams. In both the spectrum with the temporal overlap and the background spectrum in Figure 9a, a small hump structure is commonly observed at around $\Delta E = -4.1$ eV. A most probable origin of this hump structure is stray scattered electrons arriving later at the detector.

4.4. Two-Dimensional Angular Distribution

The recorded differential cross section (DCS) of the LAES signals of Ar corresponding to the energy shift of $n = +1$ in the scattering angle ranges of $1.8° \leq \theta \leq 10°$ and $-180° \leq \phi \leq 180°$ is plotted as a two-dimensional DCS histogram in Figure 10a and a one-dimensional DCS histogram at $\phi = \pm 90°$ and that at $\theta = 9.3°$ are plotted in Figure 10c,d, respectively. The experimental two-dimensional DCS spectrum shown in Figure 10a is in good agreement with the theoretical DCS shown in Figure 10b obtained using the Kroll-Watson formula [16], in which the spatial distributions of the sample gas, the electron pulses, and the laser pulses are taken into account.

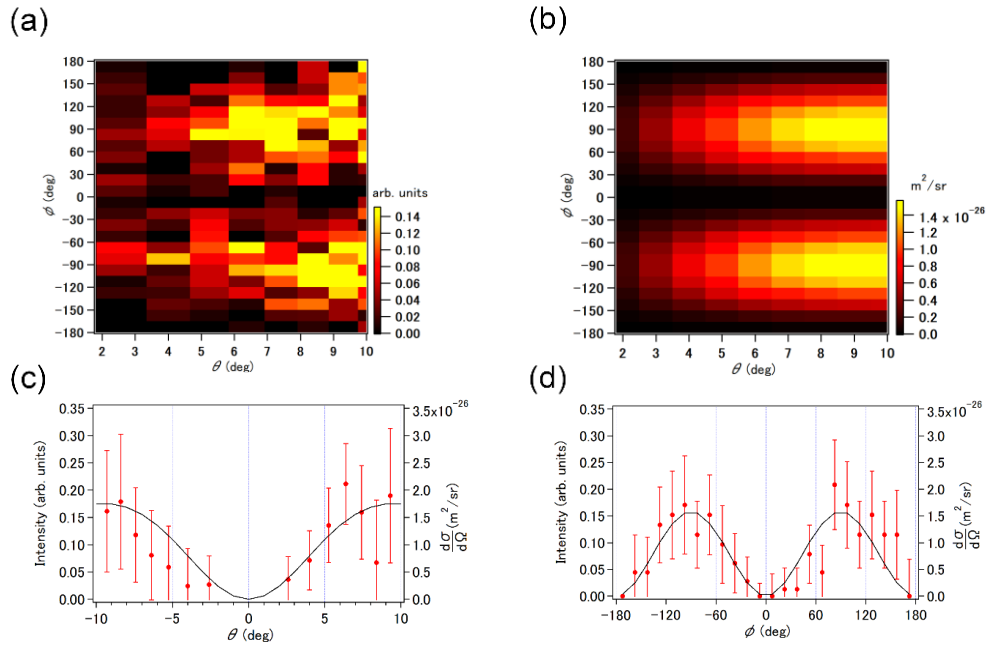

Figure 10. Angular intensity distributions of the LAES signals ($n = +1$) with an Ar gas: (**a**) Experimental two-dimensional plot. (**b**) Simulated two-dimensional plot. (**c**) Experimental (red filled circles) and simulated (black solid curve) cross sections at $\phi = \pm 90°$. The positive and negative ranges of θ correspond to $\phi = +90°$ and $-90°$, respectively. (**d**) Experimental (red filled circles) and simulated (black solid curve) cross sections at $\theta = 9.3°$.

The distribution of the DCS along the azimuthal angle ϕ exhibits two peaks at $\pm 90°$ when the polar angle θ is fixed, and the height of the two peaks increases as θ increases. The DCS of LAES of the order of n is proportional to a square of the ordinary Bessel functions ${J_n}^2(\boldsymbol{s}\cdot\boldsymbol{\alpha}_0)$ whose argument is an inner product of the momentum transfer $\boldsymbol{s} = \boldsymbol{k}_\mathrm{f} - \boldsymbol{k}_\mathrm{i}$ in a wavenumber unit and a quiver amplitude of the electron expressed by $\boldsymbol{\alpha}_0 = e\boldsymbol{\varepsilon}_0/m\omega^2$, where $\boldsymbol{\varepsilon}_0$ is laser electric field vector directing $\phi = 90°$ in the present study. Therefore, the direction of the momentum transfer is perpendicular to the polarization direction at $\phi = 0°$ or $\phi = 180°$, and consequently, the DCS of LAES becomes zero when $n \neq 0$. Under the current experimental conditions, the inner product of the quiver amplitude and the momentum transfer varies between $0.43 \leq |\boldsymbol{s}\cdot\boldsymbol{\alpha}_0| \leq 2.40$ depending on the value of θ when the azimuthal angle is fixed at $\phi = +90°$ or $\phi = -90°$. Therefore, the product of the squared Bessel function and the elastic differential cross section of an Ar atom is expected to have a local maximum at $\theta = 9.5°$, which is consistent with the increase in the DCS at $\phi = +90°$ or $\phi = -90°$ associated with the increase of θ towards 10° shown in Figure 10a,c. The two-peak structure plotted in Figure 10d can be interpreted as a structure originating from the argument of the Bessel function proportional to $\sin\phi$.

5. Summary

We have designed and constructed an apparatus equipped with the angle-resolved time-of-flight analyzer, optimized for the measurement of femtosecond LAES processes. The signal collection efficiency was raised by a factor of 40 compared with our first-generation apparatus. Using the present apparatus combined with the method of the data analysis developed also in the present study, we can record the kinetic energy distribution and the polar and azimuthal angle distribution of scattered electrons simultaneously. We performed the LAES measurements using an Ar sample gas with linearly polarized NIR laser pulses ($I = 9.0 \times 10^{11}$ W/cm^2, $\lambda = 800$ nm, $\Delta t = 40$ fs, $f = 5$ kHz) whose polarization direction is perpendicular to the direction of the electron beam pulses synchronized with the ultrashort laser pulses and recorded the LAES signals assigned to $n = \pm 1, +2$. Thanks to the improvement of signal collection efficiency, the two-dimensional angular distribution corresponding to $n = +1$ was also obtained, which shows good agreement with the theoretical distribution given by Kroll-Watson theory. The significant improvement in the detection efficiency achieved by the second-generation LAES apparatus will enable us to perform time-resolved pump-probe measurements of LAED signals and determine a temporal variation of geometrical structures of polyatomic molecules in the course of chemical bond breaking and isomerization processes with femtosecond temporal resolution.

Author Contributions: Conceptualization, R.K. and K.Y.; Methodology, R.K. and K.I.; Formal Analysis, M.I.; Investigation, M.I.; Resources, R.K and K.Y.; Writing—Original Draft Preparation, M.I.; Writing—Review and Editing, K.Y.; Visualization, M.I.; Supervision, K.Y.; Funding Acquisition, K.Y. All authors have read and agreed to the published version of the manuscript.

Funding: The present study has been supported by JSPS KAKENHI Grants Nos. 20H00371, 17H03004, 15H05696, and 26288004.

Institutional Review Board Statement: Not applicable.

Informed Consent Statement: Not applicable.

Data Availability Statement: The data presented in this study are available on request from the corresponding author.

Conflicts of Interest: The authors declare no conflict of interest.

References

1. Bunkin, F.V.; Fedorov, M. Bremsstrahlung in a strong radiation field. *Sov. Phys. JETP* **1966**, *22*, 844.
2. Mason, N.J. Laser-assisted electron-atom collisions. *Rep. Prog. Phys.* **1993**, *56*, 1275–1346. [CrossRef]
3. Weingartshofer, A.; Jung, C. Multiphoton free-free transitions. In *Multiphoton Ionization of Atoms*; Chin, S.L., Ed.; Academic Press: Toronto, ON, Canada, 1984; pp. 155–187.
4. Ehlotzky, F.; Jaroń, A.; Kamiński, J. Electron–atom collisions in a laser field. *Phys. Rep.* **1998**, *297*, 63–153. [CrossRef]
5. Andrick, D.; Langhans, L. Measurement of free-free transitions in e-Ar scattering. *J. Phys. B At. Mol. Phys.* **1976**, *9*, L459–L461. [CrossRef]
6. Langhans, L. Resonance structures in the free-free cross section of e-Ar scattering. *J. Phys. B At. Mol. Phys.* **1978**, *11*, 2361–2366. [CrossRef]
7. Andrick, D.; Bader, H. Resonance structures in the cross section for free-free radiative transitions in e-He scattering. *J. Phys. B At. Mol. Phys.* **1984**, *17*, 4549–4555. [CrossRef]
8. Bader, H. Resonance structures in the cross section for free-free radiative transitions in e-Ne and e-Ar scattering. *J. Phys. B At. Mol. Phys.* **1986**, *19*, 2177–2188. [CrossRef]
9. Weingartshofer, A.; Holmes, J.K.; Caudle, G.; Clarke, E.M.; Krüger, H. Direct Observation of Multiphoton processes in Laser-Induced Free-Free Transitions. *Phys. Rev. Lett.* **1977**, *39*, 269–270. [CrossRef]
10. Wallbank, B.; Holmes, J.K.; MacIsaac, S.C.; Weingartshofer, A. Resonance structures in free-free cross sections for electron-helium scattering. *J. Phys. B At. Mol. Opt. Phys.* **1992**, *25*, 1265–1277. [CrossRef]
11. Wallbank, B.; Holmes, J.K. Laser-assisted elastic electron-atom collisions. *Phys. Rev. A* **1993**, *48*, R2515–R2518. [CrossRef]
12. Wallbank, B.; Holmes, J.K. Laser-assisted elastic electron scattering from helium. *Can. J. Phys.* **2001**, *79*, 1237–1246. [CrossRef]
13. Nehari, D.; Holmes, J.; Dunseath, K.M.; Terao-Dunseath, M. Experimental and theoretical study of free–free electron–helium scattering in a CO_2 laser field. *J. Phys. B At. Mol. Opt. Phys.* **2010**, *43*, 25203. [CrossRef]

14. Wallbank, B.; Holmes, J.K.; Weingartshofer, A. Experimental differential cross sections for multiphoton free-free transitions. *J. Phys. B At. Mol. Phys.* **1987**, *20*, 6121–6138. [CrossRef]
15. Wallbank, B.; Holmes, J.K. Differential cross sections for laser-assisted elastic electron scattering from argon. *J. Phys. B At. Mol. Opt. Phys.* **1994**, *27*, 5405–5418. [CrossRef]
16. Kroll, N.M.; Watson, K.M. Charged-Particle Scattering in the Presence of a Strong Electromagnetic Wave. *Phys. Rev. A* **1973**, *8*, 804–809. [CrossRef]
17. Kanya, R.; Morimoto, Y.; Yamanouchi, K. Observation of Laser-Assisted Electron-Atom Scattering in Femtosecond Intense Laser Fields. *Phys. Rev. Lett.* **2010**, *105*, 123202. [CrossRef]
18. Kanya, R.; Morimoto, Y.; Yamanouchi, K. Apparatus for laser-assisted electron scattering in femtosecond intense laser fields. *Rev. Sci. Instrum.* **2011**, *82*, 123105. [CrossRef] [PubMed]
19. Byron, F.W., Jr.; Joachain, C.J. Electron-atom collisions in a strong laser field. *J. Phys. B At. Mol. Phys.* **1984**, *17*, L295–L301. [CrossRef]
20. Morimoto, Y.; Kanya, R.; Yamanouchi, K. Light-Dressing Effect in Laser-Assisted Elastic Electron Scattering by Xe. *Phys. Rev. Lett.* **2015**, *115*, 123201. [CrossRef]
21. Morimoto, Y.; Kanya, R.; Yamanouchi, K. Laser-assisted electron diffraction for femtosecond molecular imaging. *J. Chem. Phys.* **2014**, *140*, 64201. [CrossRef]
22. Kanya, R.; Yamanouchi, K. Femtosecond Laser-Assisted Electron Scattering for Ultrafast Dynamics of Atoms and Molecules. *Atoms* **2019**, *7*, 85. [CrossRef]
23. Ishida, K.; Morimoto, Y.; Kanya, R.; Yamanouchi, K. High-order multiphoton laser-assisted elastic electron scattering by Xe in a femtosecond near-infrared intense laser field: Plateau in energy spectra of scattered electrons. *Phys. Rev. A* **2017**, *95*, 023414. [CrossRef]
24. Ishida, K. Development of an Apparatus for Femtosecond Laser-Assisted Elastic Electron Scattering with High-Sensitivity and the Observation of High-Order Multiphoton Processes. Doctoral Thesis, The University of Tokyo, Tokyo, Japan, 2017. [CrossRef]
25. Park, H.; Hao, Z.; Wang, X.; Nie, S.; Clinite, R.; Cao, J. Synchronization of femtosecond laser and electron pulses with subpicosecond precision. Review of scientific instruments. *Rev. Sci. Instrum.* **2005**, *76*, 083905. [CrossRef]
26. Jablonski, A.; Salvat, F.; Powell, C.J. NIST Electron Elastic-Scattering Cross-Section Database-Version 4.0. *Natl. Inst. Stand. Technol.* **2002**. [CrossRef]